Magnon valley Hall effect in CrI₃-based van der Waals heterostructures

R. Hidalgo-Sacoto [1] R. I. Gonzalez,[2] E. E. Vogel,[3,4] S. Allende,[4,5] José D. Mella,[4,6] C. Cardenas,[4,6]
Roberto E. Troncoso,[7] and F. Munoz [4,6,*]

[1]*School of Physical Sciences and Nanotechnology, Yachay Tech, Urukuí, Ecuador*
[2]*Centro de Nanotecnología Aplicada, Facultad de Ciencias, Universidad Mayor, Santiago, Chile*
[3]*Departamento de Ciencias Físicas, Universidad de La Frontera, Temuco, Chile*
[4]*Center for the Development of Nanoscience and Nanotechnology, Santiago, Chile*
[5]*Departamento de Física, Universidad de Santiago de Chile, Santiago, Chile*
[6]*Departamento de Física, Facultad de Ciencias, Universidad de Chile, Santiago, Chile*
[7]*Center for Quantum Spintronics, Department of Physics, Norwegian University of Science and Technology, NO-7491 Trondheim, Norway*

Magnonic excitations in the two-dimensional (2D) van der Waals (vdW) ferromagnet chromium triiodide (CrI₃) are studied. We find that bulk magnons exhibit a nontrivial topological band structure without the need for Dzyaloshinskii-Moriya interaction. This is shown in vdW heterostructures, consisting of single-layer CrI₃ on different 2D materials such as MoTe₂, HfS₂, and WSe₂. We find numerically that the proposed substrates substantially modify the out-of-plane magnetic anisotropy on each sublattice of the CrI₃ subsystem. The induced staggered anisotropy, combined with a proper band inversion, leads to the opening of a topological gap of the magnon spectrum. Since the gap is opened nonsymmetrically at the $\mathbf{K}^+$ and $\mathbf{K}^-$ points of the Brillouin zone, an imbalance in the magnon population between these two valleys can be created under a driving force. This phenomenon has a close analogy to the so-called valley Hall effect and is thus termed the magnon valley Hall effect. In linear response to a temperature gradient, we quantify this effect by the evaluation of the temperature dependence of the magnon thermal Hall effect. These findings open a different avenue by adding the valley degrees of freedom besides the spin in the study of magnons.

I. INTRODUCTION

Magnons, the low-energy spin excitations of magnets, occupy a central place in the field of spintronics [1]. Since magnons carry spin angular momentum and do not possess electric charge, the understanding and control of their transport properties are of paramount importance [2,3]. From a practical perspective, the lack of charge transport, implying the absence of energy loss in the form of heat via Joule heating, is certainly attractive.

Research on topological matter inspired a plethora of theoretical predictions about topological magnons systems in recent years. Among the first proposals, it was shown that engineered magnonic crystals develop topological bulk magnon bands and hence host chiral edge states [4]. Other alternative routes exploit mechanisms based on emergent gauge fields induced by magnetic textures, e.g., Skyrmion crystals [5,6]. These magnetic phases provide a natural crystalline environment and shown that magnons inherit a topologically nontrivial band structure [7–9]. Interestingly, topological features are also present in specific lattice geometries, for example, the honeycomb [10–13], Kitaev [14–16], and kagome lattice [17–20] spin systems. In most of them, the Dzyaloshinskii-Moriya interaction (DMI) is a key element [10,21] since it

plays a role analogous to the spin-orbit coupling (SOC) in the Kane-Mele model [22]. However, theoretical studies have shown that magnonic bulk bands carry nontrivial Chern numbers under the presence of nearest-neighbor pseudodipolar interaction [23–25] and without the need for DMI.

In this work, we show that van der Waals (vdW) heterostructures, consisting of CrI₃ on different two-dimensional (2D) materials with a hexagonal lattice, open a topological gap in the magnon spectrum of the CrI₃ subsystem. Unlike previous schemes based on the DMI [10,21], our approach closely resembles an electrically induced band gap in bilayer graphene [26–29]. Symmetry arguments can establish the underlying mechanism that gives rise to this effect. The honeycomb lattice of CrI₃ has a sublattice symmetry, with two identical but nonequivalent Cr atoms [see Fig. 1(a)]. If we consider the heterostructure CrI₃|MX_2, with MX_2 being the matched hexagonal material (e.g., a transition-metal dichalcogenide), each Cr sublattice will have a different environment, and thus, the sublattice symmetry is broken. Accordingly, the octahedrons of I atoms, which wrap each Cr, are distorted differently for each sublattice. Therefore, the magnetocrystalline anisotropy energy will be different for each sublattice. It is worth commenting that this is independent of details such as the actual minimum-energy configuration. It is worth mentioning that the manipulation of the valley degree of freedom in vdW heterostructures, consisting of transition-metal dichalcogenides and magnetic substrates, such as the
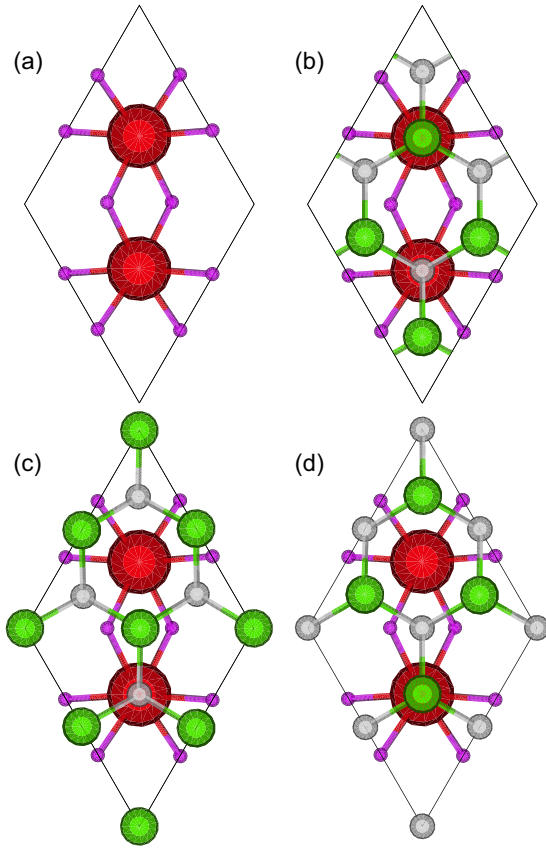
FIG. 1. (a) Top view of the unit cell of CrI_3; Cr (I) atoms are the big red (small purple) spheres. (b)–(d) Different lateral arrangements of a heterostructure formed by a hexagonal lattice and CrI_3. The medium-sized atoms belong to different sublattices of the hexagonal system: white, metal (e.g., Mo, W, and Hf) and green, chalcogen (e.g., Te, Se, and S).

ones proposed here, has experienced a great deal of interest in recent years [30–32]. Also, there exist theoretical studies [33,34] and experimental realizations [35,36] of the specific vdW heterostructures we are proposing for the magnon valley Hall effect (MVHE).

As a further step, we study the low-energy magnetic fluctuations of the effective spin system. We focus on magnonic excitations around the collinear ferromagnetic (FM) ground state, where the substrate effects appear as a staggered on-site energy added to the magnon Hamiltonian. Concretely, we construct the magnonic analog of the valley Hall effect in graphene by breaking the inversion symmetry. In order to discuss the experimental accessibility of the predicted phenomena, we study magnon transport in linear response to a thermal bias. The nontrivial Berry curvature leads to the magnon thermal Hall effect, which is determined by the calculation of the transverse thermal conductivity at finite temperature.

This paper is outlined as follows. In Sec. II we describe the numerical methods employed in this work. In Sec. III we first determine the most energetically favorable crystalline configuration between the CrI_3 layer and each of the proposed substrates. In Sec. IV we obtain all the relevant magnetic constants for the CrI_3 subsystem based on the previously

derived magnetic Hamiltonian. The magnon valley Hall effect and its effects on the transverse thermal conductivity (via the magnon thermal Hall effect) are computed. We conclude in Sec. V with a discussion of our results.

II. NUMERICAL METHODS

In this section we explain our approach for density functional theory (DFT) calculations. We use the VASP package [37–40]. The kinetic energy cutoff is set to 250 eV. We tested the effect of a larger cutoff, up to 550 eV, and the change in the magnetic anisotropies was less than a few μeV. The k-point grid is 11×11. For the exchange-correlation term, we use the Strongly-Constrained and Appropriately-Normed (SCAN) meta-generalized gradient approximation (GGA) [41] (the details of the vdW functional are below). At least 12 Å of empty vacuum space are added to avoid spurious self-interactions along the nonperiodic direction. To account for the Coulomb repulsion of Cr d electrons, we use the DFT+U formulation [42] with parameters $U = 2.7$ eV and $J = 0.6$ eV [43]; nevertheless, the values of magnetic constants are practically unaffected by these parameters (as long as the system remains insulating). The PYPROCAR code is employed for the analysis of eigenvalues [44]. We use projector augmented-wave pseudopotentials [45]. The SOC is included in all calculations, except phonons.

The calculation for the parameters of the magnetic Hamiltonian [see Eq. (2)] closely follows the procedure of Lado and Fernández-Rossier [43]. We will summarize it after introducing the spin Hamiltonian. However, the calculation of the magnetocrystalline anisotropies is more involved, and it is convenient to elaborate here the technical aspects of its calculation. The calculation of the individual anisotropy of each sublattice needs a noncollinear orientation of the magnetic moments around each Cr atom in order to explicitly break the sublattice symmetry (and hence have sublattice split anisotropies). This breaking is possible by adding an extra penalty to the energy [46]:

$$\Delta E_\epsilon = \epsilon\{[\boldsymbol{m}_a - \hat{z}(\boldsymbol{m}_a \cdot \hat{z})]^2 + [\boldsymbol{m}_b - \hat{x}(\boldsymbol{m}_b \cdot \hat{x})]^2\}, \quad (1)$$

with $\boldsymbol{m}_\alpha$ being the magnetic moment around a Cr ion of the sublattice $\alpha = \{a, b\}$, i.e., $\boldsymbol{m}_\alpha = \int_{R_\alpha} \boldsymbol{m}(\boldsymbol{r})d\boldsymbol{r}^3$ for some suitable radius R_α. The $\hat{x}$ and $\hat{z}$ axes refer to the in-plane and out-of-plane directions, respectively.

The parameter ϵ is a factor scaling related to the strength of the penalty. If ϵ is large enough, the system's ground state will be the minimum in Eq. (1); that is, $\boldsymbol{m}_a$ is along $\hat{z}$ and $\boldsymbol{m}_b$ is along $\hat{x}$. By systematically decreasing the value of ϵ, the above configuration will remain pinned, as a local minimum of energy, which can be arbitrarily shallow. Once the energy due to ΔE_ϵ is much smaller than all the other relevant energy scales, it should not affect their value. To avoid any spurious effect, we varied ϵ until ΔE_ϵ is less than 1 μeV. To get the actual anisotropies, we need an additional magnetic configuration obtained by swapping the sublattices $a \leftrightarrow b$ in Eq. (1). By subtracting the total DFT energy of both calculations, we get the difference of both site anisotropies, $D_a - D_b$ [see Eq. (2)]. Since the magnetic coupling of Cr ions is weak (e.g., its Curie temperature is just 45 K [47]) and the spurious energy of ΔE_ϵ mostly cancels out by subtracting the

total DFT energies, the convergence of the magnetocrystalline anisotropy energies with ϵ was almost immediate. A value of $\epsilon = 10$ gave almost the same anisotropies as $\epsilon = 0.01$, but to be sure we used the previous, more stringent criterion.

In a vdW system, it is crucial to have a good description of the dispersive forces. The SCAN+rVV10 approach [48], coupling the SCAN meta-GGA to the revised Vydrov and Van Voorhis energy functional [49,50], gives an accurate description of binding energies and lattice parameters of vdW materials [51]. Our criterion for stopping the structural relaxation is 0.01 eV/Å as the largest force. Our electronic convergence criterion is 10^{-10} eV. For the calculation of phonons, we used a different approach, the empirical refined density functional dispersion correction method [52]. It reproduces very well our relaxed heterostructure but is much faster. We employed the PHONOPY package [53].

III. vdW HETEROSTRUCTURES AND SPIN HAMILTONIAN

In this section, we review the CrI$_3$ lattice. We present the geometry of the proposed heterostructures and how it translates in a Heisenberg-like Hamiltonian. The driving force behind the MVHE is the change in symmetry at the atomic level due to the heterostructure.

CrI$_3$ has a honeycomb lattice; hence, two identical sublattices are formed by the Cr ions. Each Cr ion is surrounded by an octahedron formed by six iodine atoms [see Fig. 1(a)]. For the magnetic description (Heisenberg Hamiltonian), the iodine atoms can be ignored since they are nonmagnetic. However, the consequences of altering the iodine octahedron will be present in the magnetic parameters. The lattice parameter of CrI$_3$ is $a = 6.95$ Å. If it forms a heterostructure with a 2D hexagonal system with a lattice parameter $a/2$, there is only one arrangement that preserves the sublattice symmetry of CrI$_3$. However, most hexagonal 2D materials have at least two *different* sublattices (e.g., with different elements), and it is impossible to preserve the sublattice symmetry of CrI$_3$ in the composed system. The effects of this mechanism on the electronic structure of CrI$_3$ are small. It is a vdW interaction but noticeable on their magnetic properties.

Among the materials whose lattice parameter a' is nearly one half of the CrI$_3$ lattice parameter, $a' \approx a/2$, we can name several transition-metal dichalcogenides (by using the unit formula MX_2, where M is a transition metal and X is a chalcogen atom) such as molybdenum ditelluride (MoTe$_2$, $a' \approx 3.5$ Å [54]), hafnium disulfide (HfS$_2$, $a' \approx 3.6$ Å [55]), titanium diselenide (TiSe$_2$, $a' \approx 3.5$ Å [56,57]), tungsten diselenide (WSe$_2$, $a' \approx 3.3$ Å [58]), tungsten ditelluride (WTe$_2$, $a' \approx 3.5$ Å [59]), etc. Other 2D materials also fit: gallium sulfide (GaS, $a' \approx 3.6$ Å [60]) and tin sulfide (SnS$_2$, ≈ 3.6 Å [61]). It may seem surprising that several 2D materials have a lattice parameter that is almost $a/2$. However, the bonding distance in several dichalcogenides ranges from 2.7 to 2.8 Å, which coincides with the Cr-I bonding distance, 2.75 Å. Another way to understand why the lattice parameter of CrI$_3$ practically doubles the value found in several hexagonal 2D materials is to consider minimal hexagonal and honeycomb lattices, ignoring all the atomic detail and keeping only the nodes. If the nodes in both lattices are at the same distance,

TABLE I. Relative binding energy of CrI$_3$ in the different MX_2 systems (see Fig. 1). The energy is in meV per unit cell. The lowest-energy arrangement for each system is taken as the reference, i.e., 0 eV.

	Arrangement		
	B	C	D
CrI$_3$|MoTe$_2$	4.8	43.5	0.0
CrI$_3$|HfS$_2$	18.0	108.9	0.0
CrI$_3$|WSe$_2$	19.9	65.8	0.0

the lattice parameter of the honeycomb is the double of the hexagonal lattice.

In the following, we restrict our study to heterostructures of CrI$_3$ over MoTe$_2$, HfS$_2$, and WSe$_2$; see the three arrangements shown in Figs. 1(b)–1(d). Even though these materials have the same lattice and have very similar compositions (metal dichalcogenide), they produce different effects on the magnetic properties of CrI$_3$. The relative energies among these arrangements, i.e., taking the lowest-energy conformation as a reference, are given in Table I. In general, the stablest position is when a chalcogen atom is below a Cr atom and the metals are in bridge positions (arrangement D). To confirm the stability of the heterostructures in at least one case, we made a phonon calculation of the ground state of CrI$_3$|MoTe$_2$ (see Fig 2).

The spin Hamiltonian of these heterostructures is a slight variation of the one proposed by Lado and Fernández-Rossier [43]:

$$H = -\sum_{i\alpha} D_\alpha \left(S_{i\alpha}^z\right)^2 - \sum_{\langle i\alpha, j\beta \rangle} \left[\frac{J}{2} \vec{S}_{i\alpha} \cdot \vec{S}_{j\beta} + \frac{\lambda}{2} S_{i\alpha}^z S_{j\beta}^z \right], \quad (2)$$

where $\langle \cdot, \cdot \rangle$ stands for summation over next-nearest-neighbor lattice sites. The indexes i, j run over each unit cell, and α, β run over the sublattices $\{a, b\}$. The value of the spin $|\vec{S}_{i\alpha}|$ is 3/2 ($3\mu_B$ per Cr atom). The first term is the magnetocrystalline anisotropy energy, where D_α depends only on the sublattice. A
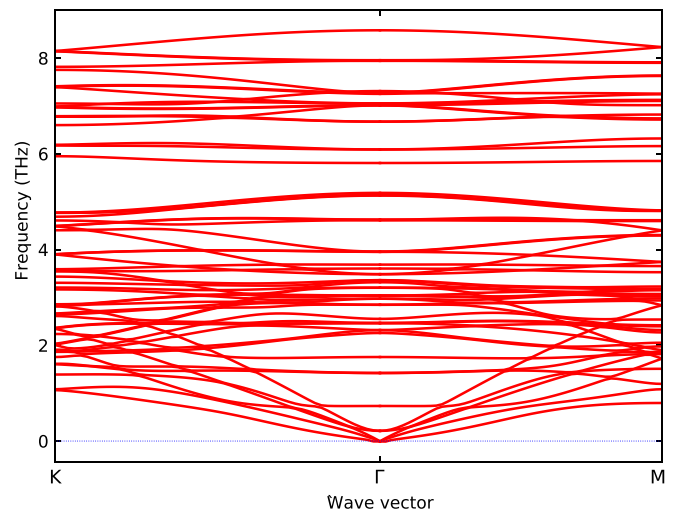

FIG. 2. Phonon dispersion of the ground-state conformation of the CrI$_3$|MoTe$_2$ heterostructure. We confirm its structural stability.

positive value of D_α implies an out-of-plane ground state. The second term is a Heisenberg Hamiltonian, with J being the exchange constant ($J > 0$ for FM interactions), and λ is the exchange anisotropy. According to Lado [43], λ is the main parameter responsible for the magnetic order of CrI$_3$.

In order to find J, λ, D_a, and D_b, we need to obtain the DFT energy of several conformations. The DFT energy can be regarded as $E_{\mathrm{DFT}} = H + H_0$, with H_0 representing all the contributions not captured by the spin Hamiltonian. Restricting the system to the CrI$_3$ unit cell (and using periodic boundary conditions), Eq. (2) has only two variables, the directions of the two nonequivalent spins, $\hat{S}_a$ and $\hat{S}_b$. Given the spin Hamiltonian $H(\hat{S}_a, \hat{S}_b)$, the energy for the relevant configurations is

$$H(\hat{z}, \hat{z}) = -\left(D_a + D_b + \frac{3J + 3\lambda}{2}\right)S^2 = E_1 - H_0, \quad (3)$$

$$H(\hat{x}, \hat{x}) = -3\frac{J}{2}S^2 = E_2 - H_0, \quad (4)$$

$$H(\hat{z}, -\hat{z}) = -\left(D_a + D_b - \frac{3J + 3\lambda}{2}\right)S^2 = E_3 - H_0, \quad (5)$$

$$H(\hat{x}, -\hat{x}) = 3\frac{J}{2}S^2 = E_4 - H_0, \quad (6)$$

$$H(\hat{x}, \hat{z}) = -D_b S^2 = E_5 - H_0, \quad (7)$$

$$H(\hat{z}, \hat{x}) = -D_a S^2 = E_6 - H_0, \quad (8)$$

from these equations and the DFT energies (E_i with $i = 1, \ldots, 6$), we can obtain the parameters of the spin Hamiltonian; for instance, subtracting Eqs. (4)–(6) gives the exchange constant J. Subtracting Eqs. (3)–(5) gives $J + \lambda$. $D_a + D_b$ can be obtained from (3), (5), (4), and (6). Finally from Eqs. (7) and (8), we can obtain $D_a - D_b$. The DFT energy corresponding to Eqs. (3)–(6) can be obtained directly. The procedure to calculate $H(\hat{x}, \hat{z})$ and $H(\hat{z}, \hat{x})$ with DFT is explained in Sec. II.

Recently, a generalization of Eq. (2) was proposed, including off-diagonal exchange coupling, but their value (in the μeV scale) is too small to be of interest here [62]. For the sake of completeness, we want to mention a recent study focused on the relevant orbitals [63] (i.e., like in a simplified tight binding), which is very useful to understand the mechanism behind the magnetism of CrI$_3$, but it is not as direct as a Heisenberg Hamiltonian to find the magnon spectrum.

The distortion due to the heterostructure also can induce different Cr-I-Cr paths, which in turn can induce a Dzyaloshinskii-Moriya coupling. We calculated the DMI vector following the scheme used by Liu *et al.* [64] for the ground state of the CrI$_3$|MoTe$_2$ heterostructure. As the geometry is similar for the other 2D materials, the order of magnitude found should also be similar. The values of the z component of the DMI vector that we obtained are smaller than 0.01 meV. Therefore, we will discard the contribution of the DMI to the magnetic Hamiltonian. Even in schemes specifically targeted to enhance DMI, its magnitude is often very small [65]. Another source of DMI comes from the contributions of higher-order neighbors, which should be quite small due to the large interatomic distances. In bulk CrI$_3$, with magnetic atoms breaking the inversion symmetry at the neighbor layer, DMI can be large enough to be experimentally observed [66].

TABLE II. Magnetic constants of CrI$_3$ on the different MX_2 systems (ground-state arrangement). All values are in meV [see Eq. (2)].

System	J	λ	D_a	D_b
CrI$_3$	2.20	0.11	0.04	0.04
CrI$_3$|MoTe$_2$	2.43	0.04	-0.18	0.33
CrI$_3$|HfS$_2$	2.05	0.13	-0.04	-0.07
CrI$_3$|WSe$_2$	2.32	0.04	0.04	0.07

The values of the magnetic constants, in the ground-state (atomic) configuration, are shown in Table II. The value of J varies only about 10% since no fundamental change in the electronic structure happens. The anisotropy λ is much more affected, decreasing to $\sim 1/3$ its value in CrI$_3$|MoTe$_2$ and CrI$_3$|WSe$_2$. This reduction is explained by the distortion on CrI$_3$ once in contact with another material; for instance, both Cr sublattices are no longer coplanar. Nevertheless, the value of λ remains positive, indicating an FM easy axis. Finally, the magnetocrystalline anisotropy suffers strong variations, especially in MoTe$_2$. The strong variations in the anisotropy constants can be expected: alterations of the symmetry of the local environment (even in vdW systems) can induce large changes, even inducing an easy axis [67]. In some of the heterostructures studied, the change in D_α also includes a change in its sign ($D_\alpha < 0$). This variation does not mean a change in easy axis since the exchange anisotropy λ dominates and is positive in every heterostructure, i.e., $|6\lambda S^2| > |D_a - D_b|S^2$ [see Eq. (9)].

IV. MAGNON VALLEY HALL EFFECT

In this section we study spin fluctuations in the limit of small deviations (magnons) around the equilibrium FM state. We consider the ground state to be collinear and parallel to the z direction. Magnonic excitations are introduced by the standard Holstein-Primakoff [68] transformation that quantizes the spins in terms of bosons [69].

The spin Hamiltonian given by Eq. (2) can be expanded up to second order in magnon operators resulting in $H = H_0 + H_m$. The zero-point energy is represented by H_0, while the nearest-neighbor tight-binding Hamiltonian for the magnonic excitations is $H_m = -\frac{JS}{2}\sum_{\langle i,j \rangle}(d_i^\dagger d_j + \mathrm{H.c.}) + \Omega \sum_i d_i^\dagger d_i$, in the absence of substrates and where $\Omega = S[2D + 3(J + \lambda)]$. The magnon operator d_i ($d_i^\dagger$) corresponds to the annihilation (creation) operator at the ith site. The Hamiltonian H_m is similar to the electronic Hamiltonian of graphene, with two Dirac points existing at $\mathbf{K}^+ = (2\pi/\sqrt{3}a, 0)$ and $\mathbf{K}^- = (-2\pi/\sqrt{3}a, 0)$ in the Brillouin zone. In CrI$_3$, a magnon gap $\Delta_0 = 3S\lambda = 0.4$ meV for the lower-energy band and critical temperature of $T_c = 85$ K are found [43]. In the presence of the proposed substrates, the Cr environment changes the magnetocrystalline anisotropy energy in each sublattice. The effect of the Hamiltonian H_m is readily captured by mapping the magnon operators into the sublattice-magnon basis,

$$H_m = -\frac{JS}{2}\sum_{\langle i,j \rangle}(a_i^\dagger b_j + \mathrm{H.c.}) + \Omega_a \sum_i a_i^\dagger a_i + \Omega_b \sum_i b_i^\dagger b_i, \quad (9)$$

where $a^\dagger$ and $b^\dagger$ represent magnon creation operators on sublattices a and b, respectively. Also, we defined $\Omega_\alpha = [2D_\alpha S + 3S(J + \lambda)]$. The induced effect by substrates on the magnon bands can be readily captured in the momentum representation. In the Fourier space, the magnon Hamiltonian reads $H_m = \sum_k \Psi_k^\dagger [\bar{\Delta}\mathbb{I} + h_k \cdot \tau]\Psi_k$, where $\Psi_k = (a_k, b_k)$ $[\Psi_k^\dagger = (a_k, b_k)^\dagger]$ is the spinor of the Fourier transformed annihilation (creation) operators, $\bar{\Delta} = (\Omega_a + \Omega_b)/2$, and τ is the Pauli matrix vector. $h_k = \sum_j (-JS\cos(k \cdot v_j), JS\sin(k \cdot u_j), \Delta)$ is a field with $\Delta = (\Omega_a - \Omega_b)/2$. The eigenenergies of the upper and lower magnon bands are given by $\epsilon_k^\pm = \bar{\Delta} \pm |h_k|$. In the limit $\Omega_a = \Omega_b$, both bands become degenerate at the Dirac points $\mathbf{K}^+$ and $\mathbf{K}^-$, with a Dirac-type dispersion around these points. In the presence of the substrates, the magnetic anisotropy becomes different on each sublattice, and a band gap is open at $\mathbf{K}^+$ ($\mathbf{K}^-$) with a value of 2Δ. It is worth noticing that the gaps open differently since $\epsilon_{\mathbf{K}^+}^\pm = \bar{\Delta} \pm \Delta$ and $\epsilon_{\mathbf{K}^-}^\pm = \bar{\Delta} \mp \Delta$. The Berry curvatures of the upper and the lower magnon bands are largely concentrated and opposite in sign around the corners of the Brillouin zone [70]. Thus, the Chern number of each band is zero [25]. However, restricting the integration zone to a single valley, around $\mathbf{K}^\pm$, the Chern number is $c_n^\pm = \int \Omega_z^\pm dk^2 = \pm 1$ [70].

Although perpendicularly magnetized honeycomb lattices with staggered anisotropy on each sublattice are topologically trivial, this represents the basic ingredient to induce an MVHE in a CrI$_3$-based vdW heterostructure. Motivated by related works on graphenelike structures [71], we consider an induced *band inversion* as a second ingredient. It consists of a sign change of the band gap obtained by, e.g., swapping the sublattices $a \leftrightarrow b$, which in turn implies swapping the anisotropy $D_a \leftrightarrow D_b$. The latter can be achieved by inducing a line defect in the MX_2 monolayer [see Fig. 3(b)]. This type of defect has been extensively studied, the most common methods to induce this inversion being those based on chalcogen defects [72–74] (see Ref. [75] and references therein). Recently, a sublattice inversion induced by irradiation was reported for MoTe$_2$ [76]. Another method to create a postsynthesis sublattice inversion is the incorporation of excess Mo atoms in MoTe$_2$. These extra Mo atoms induce a self-organization into highly ordered one-dimensional (1D) patterns that reach a length of several nanometers [77]. Another possibility to exchange the staggered anisotropies is through lateral heterostructures, which is a one-dimensional interface between two vdW materials [78]. Lateral heterostructures open new possibilities, such as a different decay length of the topological state on each side of the material.

In general the topological order of the matter implies the *bulk-boundary correspondence* [79]. When the topological order is related to the valley degree of freedom, not every border has topologically protected edge states. To illustrate this point, we have calculated two types of edges: a simple boundary (i.e., the edge of a wide nanoribbon) and a line defect swapping the staggered anisotropies. Figures 3(c) and 3(e) illustrate, in a zigzag nanoribbon without line defect, that the edges states are flat bands connecting the $\mathbf{K}^+$ and $\mathbf{K}^-$ valleys. The band gap achieved by this vdW heterostructure goes from 0.1 meV (CrI$_3$|HfS$_2$) to nearly 1.5 meV (CrI$_3$|MoTe$_2$). Specifically, we used zigzag edges since they are among
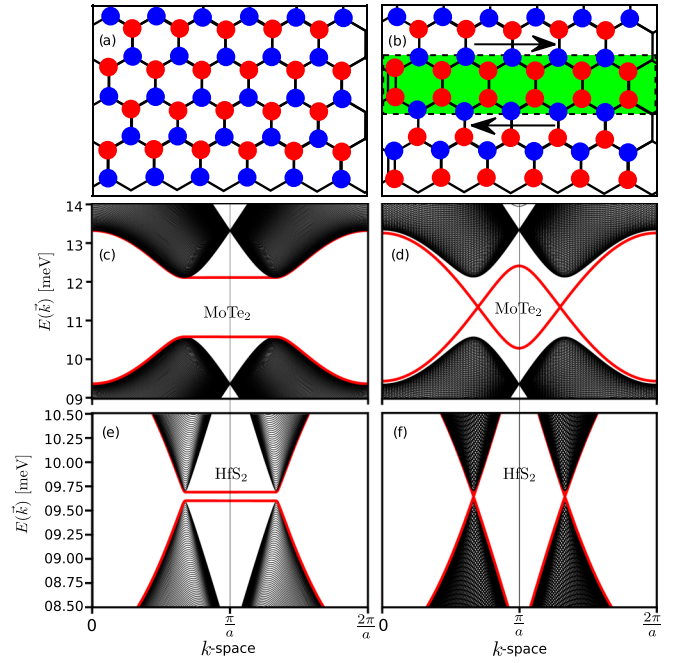

FIG. 3. (a) The bulk honeycomb lattice is formed by the Cr atoms. The colors mark the different on-site terms in Eq. (9). (b) A 1D domain wall swapping the sublattices (i.e., the on-site term in the spin Hamiltonian). The topologically protected magnon states will appear around this region. Magnon edge states (red lines) and subbands (black lines) of a finite ribbon of CrI$_3$|MoTe$_2$ and CrI$_3$|HfS$_2$ heterostructure, (c) and (e) without and (d) and (f) with a domain wall. With the domain wall, the topological edge states bridge the gap in both cases.

the nanoribbon terminations with low-energy surface states. Depending on the actual nanoribbon termination, extra edges states can appear [80]. In general, borders with nonbonding atoms (in the chemical jargon) have these edges states, and those without nonbonding atoms (such as the armchair termination) do not have low-energy edge states. See Ref. [81] for a simple explanation, and Ref. [82] for a careful derivation of the existence of these states.

When sublattice inversion is considered by introducing a line defect [Fig. 3(b)] and the condition $J/2 \geqslant |D_b - D_a|$ is fulfilled, the MVHE is presented in the system (see the Appendix). Two topologically protected states with opposite velocities at the defect line appear, connecting the valence and conduction bands [Figs. 3(d) and 3(f)]. Particularly, CrI$_3$ with all substrates meets the necessary condition to exhibit this effect. These states at the defect line (see Fig. 4) have an exponential decay that depends on the band gap induced by the substrate without the defect line. While the topological states are localized, their penetration depth is strongly dependent on the topological band gap. The localization of these states has deep consequences in the presence of disorder, breaking the sublattice symmetry (i.e., disorder in anisotropies). When the edge state penetrates several sites, the atomic disorder experienced by the localized state averages to zero, making the edge state mostly unaffected even in the case of a very large disorder [83].
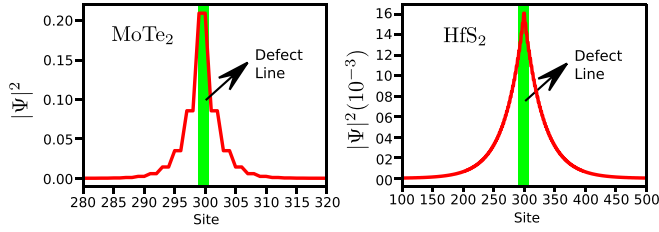
FIG. 4. Wave function of the topological protected states at defect line near projection of the $\mathbf{K}^+$ point. The left panel shows the $CrI_3|MoTe_2$ wave function (large band gap). The right panel illustrates the $CrI_3|HfS_2$ wave function (small band gap). The localization length is much larger for systems with a smaller magnon band gap.

In order to connect the MVHE with experimentally accessible measurements, we consider magnon transport in the vdW heterostructures in the presence of a thermal bias. In the linear response, we compute the magnon thermal Hall conductivity κ_{xy} [84] under a longitudinal temperature gradient. Following standard transport theory [85], we compute the thermal conductivity given by the expression $\kappa_{xy} = -k_B^2 T/h^2 \sum_{n=\pm} \int [c_2(g(\epsilon_{nk})) - \pi^2/3] \Omega_z^n(k) d\mathbf{k}$, where the sum runs over both eigenvalues $\epsilon_\pm$ and $g(\epsilon)$ is the Bose-Einstein distribution. The function c_2 [86] is a monotonous function satisfying $c_2(0) \to 0$ and $c_2(\infty) \to \pi^2/3$. The value of κ_{xy} integrated over the whole Brillouin zone is exactly zero since both valleys have opposite Berry curvatures. If we restrict the integral to a neighborhood around $\mathbf{K}^+$, we will get the contribution of each valley to the Hall thermal conductivity. The valley effect of magnons arises when a defect line swaps both sublattices, following the mechanism introduced above. In Fig. 5, we show the temperature-dependent thermal conductivity. The result of κ_{xy} for every vdW heterostructure is in the range of 10^{-3} (W/Km), close to the thermal conductivity of other topological schemes [84]. Importantly, when the temperature increases, we see a significant upturn of κ_{xy} for $CrI_3|MoTe_2$, contrary to the other heterostructures due to

their small gap. As expected, the thermal conductivity reaches a maximum value roughly at a similar critical temperature, then decays to zero for higher temperature.

V. CONCLUSIONS

In this paper, we proposed a mechanism to induce topologically nontrivial states in the magnon spectrum of a single layer of CrI_3, in analogy with the valley Hall effect in the electronic structure of bilayer graphene. The topological edge states are achieved when (i) each sublattice has a different magnetocrystalline anisotropy and (ii) there exists a region where the magnetocrystalline anisotropies of both sublattices swap. A sublattice-dependent magnetocrystalline anisotropy is obtained by forming a vdW heterostructure with another (nonmagnetic) hexagonal 2D material or substrate. The local sublattice inversion requires a line defect in the CrI_3 layer. These defects, with an extension of several nanometers, can be found naturally or can be artificially induced with great accuracy. We quantified this effect by DFT calculations of the heterostructures of CrI_3 with $MoTe_2$, HfS_2, and WSe_2.
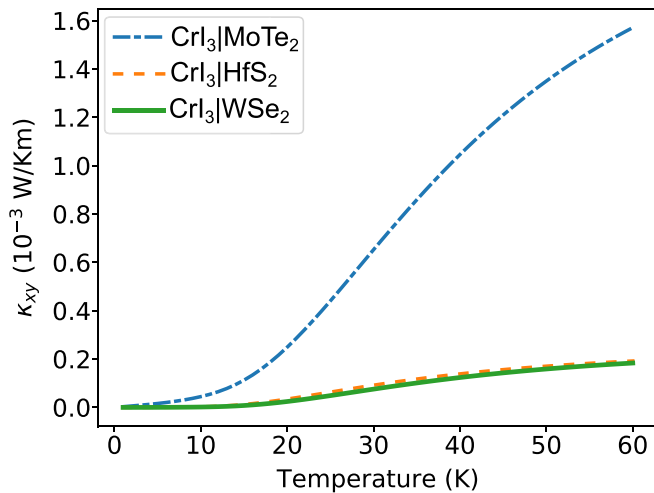

FIG. 5. Temperature-dependent magnon thermal Hall conductivity κ_{xy} for each of the proposed vdW heterostructures. A thickness of 1 nm was used to normalizes κ_{xy}. The temperature range is intentionally considered up to the critical temperature $T_C = 85$ K.
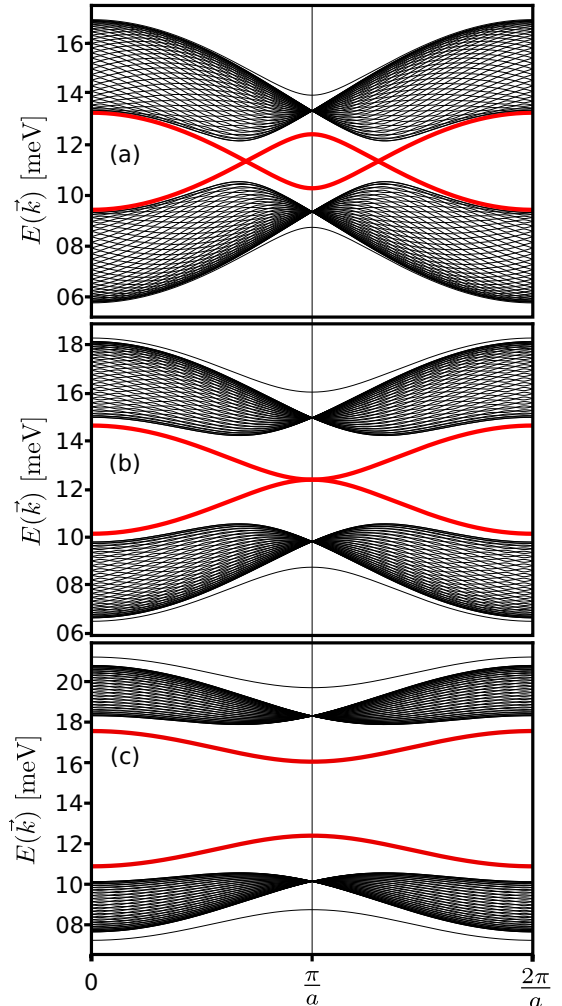

FIG. 6. Magnon dispersion due to a 1D domain wall swapping the sublattices. (a) $J/2 > |D_b - D_a|$, (b) $J/2 = |D_b - D_a|$, and (c) $J/2 < |D_b - D_a|$.

The topological band gap induced in the magnon spectrum in the previous materials ranged between 0.1 and 1.5 meV. Finally, we showed that the MVHE manifests itself in the form of a magnon thermal Hall effect due to the nontrivial topology of the band structure when a thermal gradient is applied along the heterostructure. This effect is quantified by the evaluation of the temperature-dependent transverse thermal conductivity.

APPENDIX: MAXIMUM VALUE OF STAGGERED ANISOTROPY

If the difference of the staggered anisotropy is larger than the exchange constant, $|D_b - D_a| > J/2$, the defect states due to the MVHE do not close the magnon band gap (see Fig. 6). In this case, the *hopping* cannot overcome the gap due to the anisotropies (the on-site term in tight binding).

[1] A. V. Chumak, V. I. Vasyuchka, A. A. Serga, and B. Hillebrands, Magnon spintronics, Nat. Phys. **11**, 453 (2015).

[2] V. V. Kruglyak, S. O. Demokritov, and D. Grundler, Magnonics, J. Phys. D **43**, 264001 (2010).

[3] A. A. Serga, A. V. Chumak, and B. Hillebrands, YIG magnonics, J. Phys. D **43**, 264002 (2010).

[4] R. Shindou, R. Matsumoto, S. Murakami, and J.-i. Ohe, Topological chiral magnonic edge mode in a magnonic crystal, Phys. Rev. B **87**, 174427 (2013).

[5] N. Nagaosa and Y. Tokura, Topological properties and dynamics of magnetic skyrmions, Nat. Nanotechnol. **8**, 899 (2013).

[6] A. Fert, N. Reyren, and V. Cros, Magnetic skyrmions: Advances in physics and potential applications, Nat. Rev. Mater. **2**, 17031 (2017).

[7] T. Schwarze, J. Waizner, M. Garst, A. Bauer, I. Stasinopoulos, H. Berger, C. Pfleiderer, and D. Grundler, Universal helimagnon and skyrmion excitations in metallic, semiconducting and insulating chiral magnets, Nat. Mater. **14**, 478 (2015).

[8] A. Roldán-Molina, A. S. Nunez, and J. Fernández-Rossier, Topological spin waves in the atomic-scale magnetic skyrmion crystal, New J. Phys. **18**, 045015 (2016).

[9] M. Garst, J. Waizner, and D. Grundler, Collective spin excitations of helices and magnetic skyrmions: Review and perspectives of magnonics in non-centrosymmetric magnets, J. Phys. D **50**, 293002 (2017).

[10] S. K. Kim, H. Ochoa, R. Zarzuela, and Y. Tserkovnyak, Realization of the Haldane-Kane-Mele Model in a System of Localized Spins, Phys. Rev. Lett. **117**, 227201 (2016).

[11] S. A. Owerre, A first theoretical realization of honeycomb topological magnon insulator, J. Phys.: Condens. Matter **28**, 386001 (2016).

[12] R. Cheng, S. Okamoto, and D. Xiao, Spin Nernst Effect of Magnons in Collinear Antiferromagnets, Phys. Rev. Lett. **117**, 217202 (2016).

[13] V. A. Zyuzin and A. A. Kovalev, Magnon Spin Nernst Effect in Antiferromagnets, Phys. Rev. Lett. **117**, 217203 (2016).

[14] P. A. McClarty, X.-Y. Dong, M. Gohlke, J. G. Rau, F. Pollmann, R. Moessner, and K. Penc, Topological magnons in Kitaev magnets at high fields, Phys. Rev. B **98**, 060404(R) (2018).

[15] D. G. Joshi, Topological excitations in the ferromagnetic Kitaev-Heisenberg model, Phys. Rev. B **98**, 060405(R) (2018).

[16] E. Aguilera, R. Jaeschke-Ubiergo, N. Vidal-Silva, L. Foa, and A. Núñez, Topological magnonics in the two-dimensional van der Waals magnet CrI₃, arXiv:2002.05266.

[17] R. Chisnell, J. S. Helton, D. E. Freedman, D. K. Singh, R. I. Bewley, D. G. Nocera, and Y. S. Lee, Topological Magnon Bands in a Kagome Lattice Ferromagnet, Phys. Rev. Lett. **115**, 147201 (2015).

[18] R. Seshadri and D. Sen, Topological magnons in a kagome-lattice spin system with *xxz* and Dzyaloshinskii-Moriya interactions, Phys. Rev. B **97**, 134411 (2018).

[19] S. A. Owerre, Strain-induced topological magnon phase transitions: Applications to kagome-lattice ferromagnets, J. Phys.: Condens. Matter **30**, 245803 (2018).

[20] D. Malz, J. Knolle, and A. Nunnenkamp, Topological magnon amplification, Nat. Commun. **10**, 3937 (2019).

[21] L. Zhang, J. Ren, J.-S. Wang, and B. Li, Topological magnon insulator in insulating ferromagnet, Phys. Rev. B **87**, 144101 (2013).

[22] C. L. Kane and E. J. Mele, Quantum Spin Hall Effect in Graphene, Phys. Rev. Lett. **95**, 226801 (2005).

[23] X. S. Wang, Y. Su, and X. R. Wang, Topologically protected unidirectional edge spin waves and beam splitter, Phys. Rev. B **95**, 014435 (2017).

[24] X. S. Wang, H. W. Zhang, and X. R. Wang, Topological Magnonics: A Paradigm for Spin-Wave Manipulation and Device Design, Phys. Rev. Appl. **9**, 024029 (2018).

[25] X. S. Wang and X. R. Wang, Anomalous magnon Nernst effect of topological magnonic materials, J. Phys. D **51**, 194001 (2018).

[26] F. Munoz, H. P. O. Collado, G. Usaj, J. O. Sofo, and C. A. Balseiro, Bilayer graphene under pressure: Electron-hole symmetry breaking, valley Hall effect, and Landau levels, Phys. Rev. B **93**, 235443 (2016).

[27] E. McCann and M. Koshino, The electronic properties of bilayer graphene, Rep. Prog. Phys. **76**, 056503 (2013).

[28] L. Ju, Z. Shi, N. Nair *et al.*, Topological valley transport at bilayer graphene domain walls, Nature (London) **520**, 650 (2015).

[29] J. Xu, T. Zhu, Y. K. Luo, Y.-M. Lu, and R. K. Kawakami, Strong and Tunable Spin-Lifetime Anisotropy in Dual-Gated Bilayer Graphene, Phys. Rev. Lett. **121**, 127703 (2018).

[30] X. Xue, X. Wang, and W. Mi, Valley and spin splitting in monolayer TX_2/antiferromagnetic MnO (T=Mo, W; X=S, Se) van der Waals heterostructures, J. Phys. D: Appl. Phys. **52**, 115303 (2019).

[31] T. Habe and M. Koshino, Anomalous Hall effect in $2H$-phase MX_2 transition-metal dichalcogenide monolayers on ferromagnetic substrates (M = Mo, W, and X = S, Se, Te), Phys. Rev. B **96**, 085411 (2017).

[32] N. Cortés, O. Ávalos-Ovando, L. Rosales, P. A. Orellana, and S. E. Ulloa, Tunable Spin-Polarized Edge Currents in Proximitized Transition Metal Dichalcogenides, Phys. Rev. Lett. **122**, 086401 (2019).

[33] K. Zollner, P. E. Faria Junior, and J. Fabian, Proximity exchange effects in $MoSe_2$ and WSe_2 heterostructures with CrI_3: Twist angle, layer, and gate dependence, Phys. Rev. B **100**, 085128 (2019).

[34] C. Lin, Y. Li, Q. Wei, Q. Shen, Y. Cheng, and W. Huang, Enhanced valley splitting of transition-metal dichalcogenide by vacancies in robust ferromagnetic insulating chromium trihalides, ACS Appl. Mater. Interfaces **11**, 18858 (2019).

[35] D. Zhong, K. L. Seyler, X. Linpeng, R. Cheng, N. Sivadas, B. Huang, E. Schmidgall, T. Taniguchi, K. Watanabe, M. A. McGuire, W. Yao, D. Xiao, K.-M. C. Fu, and X. Xu, Van der Waals engineering of ferromagnetic semiconductor heterostructures for spin and valleytronics, Sci. Adv. **3**, e1603113 (2017).

[36] K. L. Seyler, D. Zhong, B. Huang, X. Linpeng, N. P. Wilson, T. Taniguchi, K. Watanabe, W. Yao, D. Xiao, M. A. McGuire, K.-M. C. Fu, and X. Xu, Valley manipulation by optically tuning the magnetic proximity effect in WSe_2/CrI_3 heterostructures, Nano Lett. **18**, 3823 (2018).

[37] G. Kresse and J. Hafner, *Ab initio* molecular dynamics for liquid metals, Phys. Rev. B **47**, 558(R) (1993).

[38] G. Kresse and J. Hafner, *Ab initio* molecular-dynamics simulation of the liquid-metal–amorphous-semiconductor transition in germanium, Phys. Rev. B **49**, 14251 (1994).

[39] G. Kresse and J. Furthmüller, Efficiency of *ab-initio* total energy calculations for metals and semiconductors using a plane-wave basis set, Comput. Mater. Sci. **6**, 15 (1996).

[40] G. Kresse and J. Furthmüller, Efficient iterative schemes for *ab initio* total-energy calculations using a plane-wave basis set, Phys. Rev. B **54**, 11169 (1996).

[41] J. Sun, A. Ruzsinszky, and J. P. Perdew, Strongly Constrained and Appropriately Normed Semilocal Density Functional, Phys. Rev. Lett. **115**, 036402 (2015).

[42] A. I. Liechtenstein, V. I. Anisimov, and J. Zaanen, Density-functional theory and strong interactions: Orbital ordering in Mott-Hubbard insulators, Phys. Rev. B **52**, R5467(R) (1995).

[43] J. L. Lado and J. Fernández-Rossier, On the origin of magnetic anisotropy in two dimensional CrI_3, 2D Mater. **4**, 035002 (2017).

[44] U. Herath, P. Tavadze, X. He, E. Bousquet, S. Singh, F. Muñoz, and A. H. Romero, Pyprocar: A Python library for electronic structure pre/post-processing, Comput. Phys. Commun. **251**, 107080 (2019).

[45] G. Kresse and D. Joubert, From ultrasoft pseudopotentials to the projector augmented-wave method, Phys. Rev. B **59**, 1758 (1999).

[46] The VASP manual: Constrained local moments approach, https://www.vasp.at/wiki/index.php/I_CONSTRAINED_M.

[47] B. Huang, G. Clark, E. Navarro-Moratalla, D. R. Klein, R. Cheng, K. L. Seyler, D. Zhong, E. Schmidgall, M. A. McGuire, D. H. Cobden, W. Yao, D. Xiao, P. Jarillo-Herrero, and X. Xu, Layer-dependent ferromagnetism in a van der Waals crystal down to the monolayer limit, Nature (London) **546**, 270 (2017).

[48] H. Peng, Z.-H. Yang, J. P. Perdew, and J. Sun, Versatile van der Waals Density Functional Based on a Meta-Generalized Gradient Approximation, Phys. Rev. X **6**, 041005 (2016).

[49] R. Sabatini, T. Gorni, and S. de Gironcoli, Nonlocal van der Waals density functional made simple and efficient, Phys. Rev. B **87**, 041108(R) (2013).

[50] O. A. Vydrov and T. Van Voorhis, Nonlocal van der Waals density functional: The simpler the better, J. Chem. Phys. **133**, 244103 (2010).

[51] S. A. Tawfik, T. Gould, C. Stampfl, and M. J. Ford, Evaluation of van der Waals density functionals for layered materials, Phys. Rev. Mater. **2**, 034005 (2018).

[52] S. Grimme, J. Antony, S. Ehrlich, and H. Krieg, A consistent and accurate ab initio parametrization of density functional dispersion correction (DFT-D) for the 94 elements H-Pu, J. Chem. Phys. **132**, 154104 (2010).

[53] A. Togo and I. Tanaka, First principles phonon calculations in materials science, Scr. Mater. **108**, 1 (2015).

[54] A. Roy, H. C. P. Movva, B. Satpati, K. Kim, R. Dey, A. Rai, T. Pramanik, S. Guchhait, E. Tutuc, and S. K. Banerjee, Structural and electrical properties of $MoTe_2$ and $MoSe_2$ grown by molecular beam epitaxy, ACS Appl. Mater. Interfaces **8**, 7396 (2016).

[55] B. Zheng, Y. Chen, Z. Wang, F. Qi, Z. Huang, X. Hao, P. Li, W. Zhang, and Y. Li, Vertically oriented few-layered HfS_2 nanosheets: Growth mechanism and optical properties, 2D Mater. **3**, 035024 (2016).

[56] C. Riekel, Structure refinement of $TiSe_2$ by neutron diffraction, J. Solid State Chem. **17**, 389 (1976).

[57] Z.-G. Fu, Z.-Y. Hu, Y. Yang, Y. Lu, F.-W. Zheng, and P. Zhang, Modulation of doping and biaxial strain on the transition temperature of the charge density wave transition in 1T-$TiSe_2$, RSC Adv. **6**, 76972 (2016).

[58] W. J. Schutte, J. L. De Boer, and F. Jellinek, Crystal structures of tungsten disulfide and diselenide, J. Solid State Chem. **70**, 207 (1987).

[59] A. Mar, S. Jobic, and J. A. Ibers, Metal-metal vs tellurium-tellurium bonding in WTe_2 and its ternary variants $TaIrTe_4$ and $NbIrTe_4$, J. Am. Chem. Soc. **114**, 8963 (1992).

[60] A. R. Barron, MOCVD of group III chalcogenides, Adv. Mater. Opt. Electron. **5**, 245 (1995).

[61] J. M. Gonzalez and I. I. Oleynik, Layer-dependent properties of SnS_2 and $SnSe_2$ two-dimensional materials, Phys. Rev. B **94**, 125443 (2016).

[62] I. Lee, F. G. Utermohlen, D. Weber, K. Hwang, C. Zhang, J. van Tol, J. E. Goldberger, N. Trivedi, and P. C. Hammel, Fundamental Spin Interactions Underlying the Magnetic Anisotropy in the Kitaev Ferromagnet CrI_3, Phys. Rev. Lett. **124**, 017201 (2020).

[63] I. V. Kashin, V. V. Mazurenko, M. I. Katsnelson, and A. N. Rudenko, Orbitally-resolved ferromagnetism of monolayer CrI$_3$, 2D Mater. **7**, 025036 (2020).

[64] J. Liu, M. Shi, J. Lu, and M. P. Anantram, Analysis of electrical-field-dependent Dzyaloshinskii-Moriya interaction and magnetocrystalline anisotropy in a two-dimensional ferromagnetic monolayer, Phys. Rev. B **97**, 054416 (2018).

[65] S. Ghosh, N. Stoji, and N. Binggeli, Structural and magnetic response of CrI$_3$ monolayer to electric field, Physica B (Amsterdam, Neth.) **570**, 166 (2019).

[66] L. Chen, J.-H. Chung, B. Gao, T. Chen, M. B. Stone, A. I. Kolesnikov, Q. Huang, and P. Dai, Topological Spin Excitations in Honeycomb Ferromagnet CrI$_3$, Phys. Rev. X **8**, 041028 (2018).

[67] F. Muñoz, J. Mejía-López, T. Pérez-Acle, and A. H. Romero, Uniaxial magnetic anisotropy energy of Fe wires embedded in carbon nanotubes, ACS Nano **4**, 2883 (2010).

[68] T. Holstein and H. Primakoff, Field dependence of the intrinsic domain magnetization of a ferromagnet, Phys. Rev. **58**, 1098 (1940).

[69] The Holstein-Primakoff transformation is defined by $S_i^+ = \sqrt{2S - d_i^\dagger d_i} d_i$, $S_i^- = d_i^\dagger \sqrt{2S - d_i^\dagger d_i}$, and $S_i^z = (S - d_i^\dagger d_i)$, with S being the spin quantum number. One magnon is created (annihilated) at site i of the lattice by the operator $d_i^\dagger$ (d_i). It corresponds to changing the total spin with $+\hbar$ ($-\hbar$).

[70] The Berry curvature of each band is calculated from $\mathbf{\Omega}^\pm = \mp \hat{\mathbf{h}} \cdot (\partial_{k_x}\hat{\mathbf{h}} \times \partial_{k_y}\hat{\mathbf{h}})/2$. Expanding around $\mathbf{K}^+$, the only nonzero components of the Berry curvature are $\Omega_z^\pm = \pm\frac{3}{4}(aJS)^2 \Delta[3(aJS)^2(q_x^2 + q_y^2)/4 + \Delta^2]^{-3/2}$. The Chern number c_n is the integral of the Berry curvature along the Brillouin zone, which is zero because the contributions around each valley cancel. However, if we restrict the integration zone to only a single valley, let's say close to $\mathbf{K}^+$, we can calculate its Chern number, $c_n^\pm = \int \Omega_z^\pm dk^2 = \pm 1$.

[71] W. Yao, S. A. Yang, and Q. Niu, Edge States in Graphene: From Gapped Flat-Band to Gapless Chiral Modes, Phys. Rev. Lett. **102**, 096801 (2009).

[72] C. J. Alvarez, M. T. Dau, A. Marty, C. Vergnaud, H. Le Poche, P. Pochet, M. Jamet, and H. Okuno, Impact of a van der Waals interface on intrinsic and extrinsic defects in an MoSe$_2$ monolayer, Nanotechnology **29**, 425706 (2018).

[73] M. Schleberger and J. Kotakoski, 2D material science: Defect engineering by particle irradiation, Materials **11**, 1885 (2018).

[74] H.-P. Komsa, S. Kurasch, O. Lehtinen, U. Kaiser, and A. V. Krasheninnikov, From point to extended defects in two-dimensional MoS$_2$: Evolution of atomic structure under electron irradiation, Phys. Rev. B **88**, 035301 (2013).

[75] M. Batzill, Mirror twin grain boundaries in molybdenum dichalcogenides, J. Phys.: Condens. Matter **30**, 493001 (2018).

[76] K. Elibol, T. Susi, G. Argentero, M. Reza Ahmadpour Monazam, T. J. Pennycook, J. C. Meyer, and J. Kotakoski, Atomic structure of intrinsic and electron-irradiation-induced defects in MoTe$_2$, Chem. Mater. **30**, 1230 (2018).

[77] P. M. Coelho, H.-P. Komsa, H. Coy Diaz, Y. Ma, A. V. Krasheninnikov, and M. Batzill, Post-synthesis modifications of two-dimensional MoSe$_2$ or MoTe$_2$ by incorporation of excess metal atoms into the crystal structure, ACS Nano **12**, 3975 (2018).

[78] O. Ávalos-Ovando, D. Mastrogiuseppe, and S E Ulloa, Lateral heterostructures and one-dimensional interfaces in 2D transition metal dichalcogenides, J. Phys.: Condens. Matter **31**, 213001 (2019).

[79] R. S. K. Mong and V. Shivamoggi, Edge states and the bulk-boundary correspondence in Dirac Hamiltonians, Phys. Rev. B **83**, 125109 (2011).

[80] J. Li, I. Martin, M. Büttiker, and A. F. Morpurgo, Marginal topological properties of graphene: A comparison with topological insulators, Phys. Scr. **2012**, 014021 (2012).

[81] A. M. Pendás, J. Contreras-García, F. Pinilla, J. D. Mella, C. Cardenas, and F. Muñoz, A chemical theory of topological insulators, Chem. Commun. **55**, 12281 (2019).

[82] P. Delplace, D. Ullmo, and G. Montambaux, Zak phase and the existence of edge states in graphene, Phys. Rev. B **84**, 195452 (2011).

[83] F. Munoz, F. Pinilla, J. Mella, and M. I. Molina, Topological properties of a bipartite lattice of domain wall states, Sci. Rep. **8**, 1 (2018).

[84] P. Laurell and G. A. Fiete, Magnon thermal Hall effect in kagome antiferromagnets with Dzyaloshinskii-Moriya interactions, Phys. Rev. B **98**, 094419 (2018).

[85] R. Matsumoto, R. Shindou, and S. Murakami, Thermal Hall effect of magnons in magnets with dipolar interaction, Phys. Rev. B **89**, 054420 (2014).

[86] The function c_2 is defined as $c_2(x) = (1 + x)[\ln(\frac{1+x}{x})]^2 - [\ln(x)]^2 - 2\text{Li}_2(-x)$, where Li_n is the polylogarithm function.

[87] X. Zhai and Y. M. Blanter, Topological Valley Transport of Gapped Dirac Magnons in Bilayer Ferromagnetic Insulators, arXiv:2002.00446v1.